Computer Simulation and Experimental Studies of SAR Distributions of Interstitial Arrays of Sleeved-Slot Microwave Antennas for Hyperthermia Treatment of Brain Tumors

James C. Lin, *Fellow, IEEE*, Shinji Hirai, Chin-Lin Chiang, Wen-Lin Hsu, Jenn-Lung Su, *Member, IEEE*, and Yu-Jin Wang

Abstract—The specific-absorption-rate (SAR) distributions produced by three-, six-, and seven-element arrays of sleeved-slot interstitial antennas in brain-equivalent tissues are investigated in this paper. Computer simulations of SAR distributions are compared to experimental measurement made in a brain-equivalent gel phantom at 2450 MHz. Results showed that a 15-mm antenna spacing would produce SAR patterns with the least variation in its distribution compared to smaller or larger spacings. Moreover, the region of elevated SARs is inscribed by the array and extends 35 mm in length to include the distal antenna-tip region. In addition, results indicate that a hexagonal array configuration of either six or seven sleeved-slot interstitial antennas could provide elevated SARs in brain tissues. Since the six-element configuration uses one less interstitial antenna with comparable SARs, it offers a better scheme for hyperthermia treatment of brain tumors.

Index Terms—Interstitial hyperthermia, microwave, SAR, sleeved-slot antenna, triangular and hexagonal arrays.

I. INTRODUCTION

HYPERTHERMIA cancer therapy is often used in conjunction with chemotherapy and radiotherapy since the cytotoxic effect of antitumor drugs is enhanced and the cell-killing ability of ionizing radiation is potentiated by hyperthermia [1]–[3]. Nevertheless, hyperthermia is still an experimental treatment in the U.S. for late-stage patients with advance or recurrent tumors, but it has gained some acceptance in Europe and Japan [4], [5], [6]. Clinical and laboratory results indicate that its efficacy depends on the induction of a sufficient temperature rise throughout the tumor volume. Accordingly, there has been increasing interest in interstitial hyperthermia

J. C. Lin, S. Hirai, C.-L. Chiang, and Y.-J. Wang are with the Department of Bioengineering and Electrical Engineering and Computer Science, University of Illinois at Chicago, Chicago, IL 60607-7053 USA (e-mail: lin@uic.edu).

W.-L. Hsu is with the Department of Radiation Oncology, Tri-Service General Hospital, Taipei, Taiwan, R.O.C.

J.-L. Su is with the Department of Biomedical Engineering, Chung Yuan Christian University, Chung Li, Taiwan, ROC.

treatment of brain tumors with control of spatial temperature uniformity within a centimeter [6]–[10].

This paper describes, through phantom modeling experiment and computer simulation, the use of triangular arrays of interstitial sleeved-slot microwave antennas in producing specific absorption rate (SAR) in brain tissues. Vector summations of electromagnetic fields radiated from a series of infinitesimal dipoles are applied to calculate the SAR patterns in tissue. SAR measurements are made in brain-equivalent gel phantom. The measured and computed SAR distributions of three-, six-, and seven-element arrays are assessed using brain-equivalent tissue models. Note that the sleeved-slot microwave antenna is designed to operate at 2450 MHz. It features improved power deposition at the tip and along the axial length of the antenna. The sleeved-slot antenna minimizes reflected current flowing up the transmission line. These features distinguish the sleeved-slot antenna from a number of existing microwave catheter antennas, which tend to produce a cold spot or low heating zone near the distal tip of the antenna [1], [2], [11]. For many clinical applications, existing protocols require insertion of the tip of the antenna well beyond the tumor boundary, creating a potential for unnecessary damage or necrosis in normal tissue. (A schematic diagram of a microwave interstitial hyperthermia system given in Fig. 1).

It is noted that, in clinical practice, the quantity of ultimate interest is temperature distribution inside the tumor. However, SAR distribution in tissue provides the driving power responsible for tissue temperature elevation over a given period of time. Moreover, in order to conduct a full investigation of the dynamic temperature variation, one needs to take into account tissue composition, blood perfusion, heat conduction effects of various tissues, and heat generation due to metabolic processes. Indeed, temperature distribution produced by the interstitial sleeved slot antenna arrays is a subject currently being assessed in our research to arrive at an optimal condition for a sufficiently uniform heating pattern both in phantom and animal models. We plan to provide the results obtained using the SAR distributions from the present investigation in a future paper.
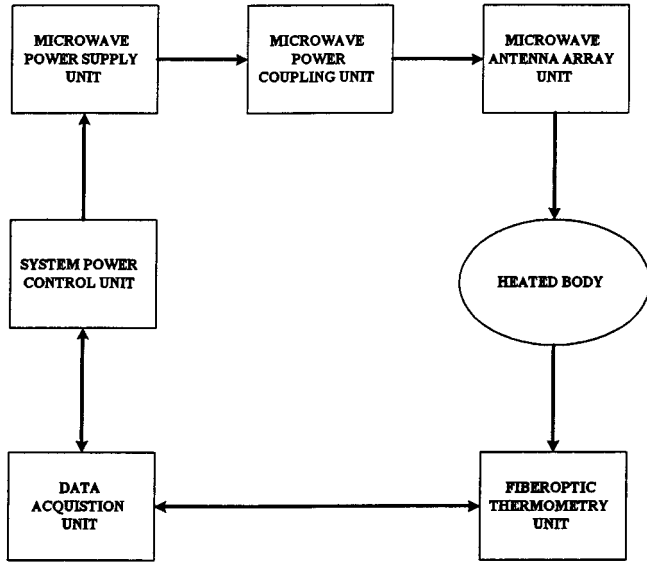
Fig. 1.   Schematic diagram of a microwave interstitial hyperthermia system.
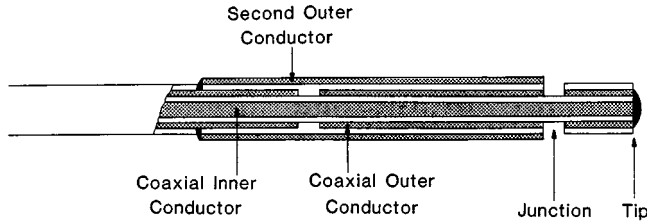

Fig. 2.   Schematic diagram of the sleeved-slot antenna. The choke sleeve was short circuited at the proximal end to the coaxial outer conductor.

II. Materials and Methods

A. Interstitial Antennas

The sleeved-slot antenna was configured with two circumferential slots and a second outer conductor that served as a current-restricting choke to prevent reflected current from flowing up the transmission line and returning to the air–phantom interface [11]. The choke sleeve was short circuited at the proximal end to the coaxial outer conductor (Fig. 2). The miniature interstitial antenna was mounted on a semirigid coaxial cable (0.86-mm OD), which serves as the transmission line for power delivery to the antenna. For 2450-MHz operation, the antenna was 20 mm in length and about 1 mm in diameter with a 3-mm tip and a 1-mm junction. The SAR pattern produced in a homogeneous tissue phantom is pear shaped, about 25 mm in length, with enhanced power deposition toward the distal end of the antenna (Fig. 3). The sleeve/choke matched the antenna to the coaxial transmission line and it helped to prevent reflected currents from flowing up the coaxial cable to the body surface. The SAR produced by the sleeved-slot antenna is independent of insertion depth so long as the depth is greater than the antenna length.

B. Computer Simulation

The computational scheme used to calculate SAR distribution assumes the sleeved-slot antenna to be a series of short segments. As long as each segment can be regarded as small com-
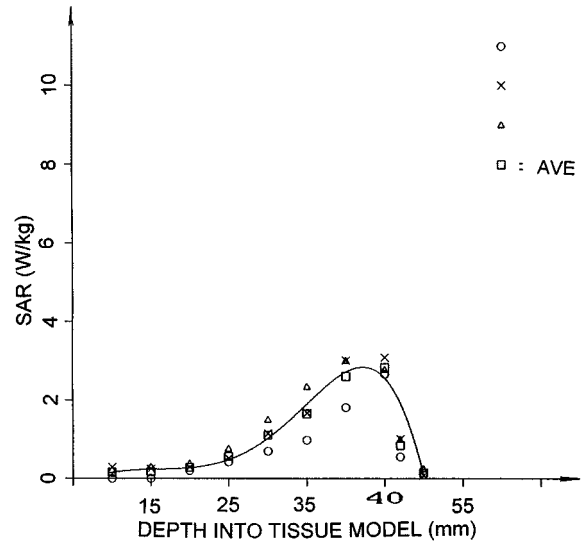

Fig. 3.   Measured longitudinal SAR pattern produced by a 2450-MHz sleeved-slot antenna in a homogeneous brain tissue phantom.

pared to the wavelength at 2450 MHz, the electric field radiated from a segment can be obtained through the dipole theory [12]. This procedure had been shown to provide fairly accurate SAR distributions in tissue medium [13]. Accordingly, for each segment, the electric field at a point inside the tissue was given by

$$E_r = \left[\eta I \ell\right]/(2\pi r^2)\left[1 + 1/(jkr)\right]e^{-jkr} \tag{1}$$

$$E_\theta = \left[j\eta I \ell\right]/(2\lambda r)\left[1 + 1/(jkr) - 1/(2k^2 r^2)\right]\sin\theta e^{-jkr} \tag{2}$$

$$E_\phi = 0 \tag{3}$$

where η is impedance of medium (Ω), I is current amplitude (in amperes), ℓ is length of a segment (in meters), k is the wavenumber (1/m), and λ is the wavelength (in meters). The antenna current was derived from measured power deposition near the surface of the antenna.

By applying the above equations repeatedly and by vector summation of field components emanating from each segment, we obtained the electric field at any point as

$$|E|^2 = \left[|E_r|^2 + |E_\theta|^2\right]^{1/2}. \tag{4}$$

For the equilateral triangular array, antennas are assumed to have the same current amplitude and are in-phase. The electric field at a point in the tissue was obtained by summation of contributions from each of the three antennas. A computational grid size of 0.5 mm was used to perform the electric-field calculations. The SAR was calculated by using

$$\mathrm{SAR} = (\sigma|E|^2)/(2\rho) \tag{5}$$

where E is the electric field (volts per meter), ρ is the density of tissue (kilograms per meters^3), and σ is the conductivity of tissue (siemens per meter).

To avoid boundary effects on the hexagonal array computations, the model volume was chosen to be $60 \times 60 \times 50$ mm for six- and seven-element hexagonal arrays (Fig. 4). These dimensions were three to four times greater than the intercatheter
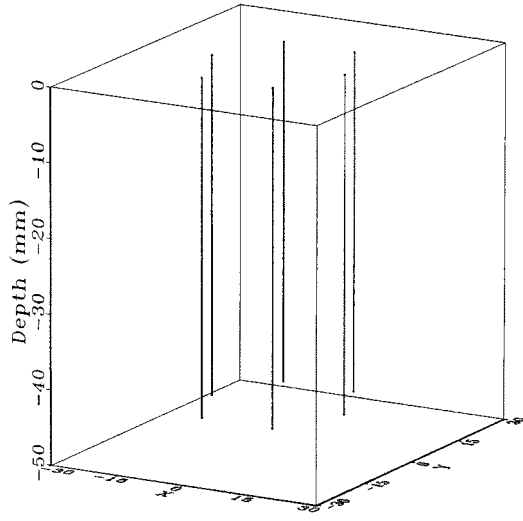
SIX ANTENNA ARRAY POSITION

Fig. 4. Configurations a six- or seven-element hexagonal array.

TABLE I
VARIATION OF SAR (IN WATTS PER KILOGRAM) AT TWO LOCATIONS WITHIN
THE ACTIVE REGION OF EQUILATERAL TRIANGLE ARRAYS

Longitudinal Position (mm)	Array Spacing (mm)								
	10			15			20		
	SUR SAR	CEN SAR	CEN/ SUR	SUR SAR	CEN SAR	CEN/ SUR	SUR SAR	CEN SAR	CEN/ SUR
25	19.9	105.3	5.3	42.2	43.1	1.0	31.9	11.5	0.4
30	26.4	192.6	7.3	64.9	67.3	1.0	56.1	22.7	0.4
35	47.0	297.9	6.3	107.4	124.6	1.2	90.0	34.8	0.4
40	71.6	372.3	5.2	127.9	150.9	1.2	113.1	37.3	0.3
45	100	245.7	2.5	100	83.5	0.8	100	83.5	0.8
50	16.7	32.5	2.0	28.2	12.5	0.4	13.4	6.22	0.5
Average	46.9	207.7	4.4	78.4	80.3	0.9	67.4	37.7	0.5

(SUR at 1 mm from antenna surface; CEN at center of triangle array. Tip of antenna is at 45 mm. Values shown are for SAR = 100 W/kg at 45 mm SUR.)

spacing in the transverse plane. Our experience showed that by locating the boundaries at these distances, reflections were reduced below 0.01%. The input power to each antenna was assumed to have equal amplitude and phase. SAR distributions were calculated from the computed electric field using tissue electrical conductivity for brain tissue (2.3 S/m) [14]. In the case of seven-element arrays, a central antenna was added to the alignment.

C. SAR Measurement in Brain Phantom

The brain phantom used for SAR measurement consisted of a glass cylinder (80-mm ID) of brain-equivalent gel dielectric [15] immersed in a constant temperature (37 °C) water bath. A Plexiglas template with predrilled holes was used to guide the implantation of Teflon catheters (1-mm ID) to the desired depth (45 mm) in the phantom. Sleeved-slot microwave antennas and Fibroptic temperature sensors (Luxtron; 1-mm diameter) were then inserted into the Teflon catheters. A triangular array was formed by locating catheters at the corners of an equilateral triangle, whose spacings varied from 10 to 20 mm.

The antennas were driven in phase and the input 2450-MHz power was 20 W to each antenna. The higher (20 W) power is used to guarantee a sufficient and necessary linear rise in temperature during a brief period of microwave application. A micromanipulator was used to position the Fibroptic sensors for measurement of temperatures at multiple points in three dimensions. (Sensors were moved manually with the assistance of the micromanipulator, in 5-mm steps, within the catheter lumen for measuring temperature at different depths.) Temperature rises were monitored and recorded every second. After the experiment, temperature rise was converted to SAR in watts per kilogram using the formula

$$\mathrm{SAR} = c(\Delta\tau/\Delta t) \qquad (6)$$

where c is the specific heat in joules per kilogram-degrees Celsius, and $\Delta\tau, \Delta t$ are the linear transient rise in temperature (de-

grees Celsius) and the brief duration (initial 10 s) of power application, respectively. Contours of constant SAR were computed using linear interpolation between measurement points.

In order to ascertain their relative advantages, measurements were conducted for both the six- and seven-element hexagonal arrays. As shown in the following section, results from the study using equilateral triangle arrays indicated the 15-mm spacing gave rise to a most uniform SAR distribution by these antennas, the 15-mm array spacing was, therefore, chosen for the hexagonal array studies.

III. RESULTS

A. Triangular Arrays

A summary of computed results for triangular arrays with 10-, 15-, or 20-mm spacing is given in Table I. The SAR values are adjusted for a 100-W/kg SAR at a point 1 mm away from the antenna surface in the tip plane (45 mm) of the antenna array. It can be seen that there are discernible variations in the computed SAR distribution in each case. The average ratio between the SAR at the center of the triangular array and a point 1 mm away from the antenna surface is 4.4 (2.0–7.3) for 10-mm spacing and 0.5 (0.3–0.8) for 20-mm spacing. However, for 15-mm spacing, the average CEN/SUR SAR ratio is 0.9 (0.4–1.2) along the active length (from 25 to 45 mm) of the antenna array. Computed SAR distributions at all cross sections for the 15-mm array showed comparable SARs at the array center and near the antennas. Thus, SAR variation is the lowest for the 15-mm array. As shown in Table I, SAR (372 W/kg) along the center for the 10-mm array was greater than anywhere else for this array configuration, while that for the 20-mm array had its highest SAR value (113 W/kg) close to the antenna surface. Similarly, the peak SAR for the 10-mm array was about 2.5 times higher than that for the 20-mm array. In addition, SAR at the center was greater than points close to the antenna surface for the 10-mm array, while it was the highest near the antennas for the 20-mm array.
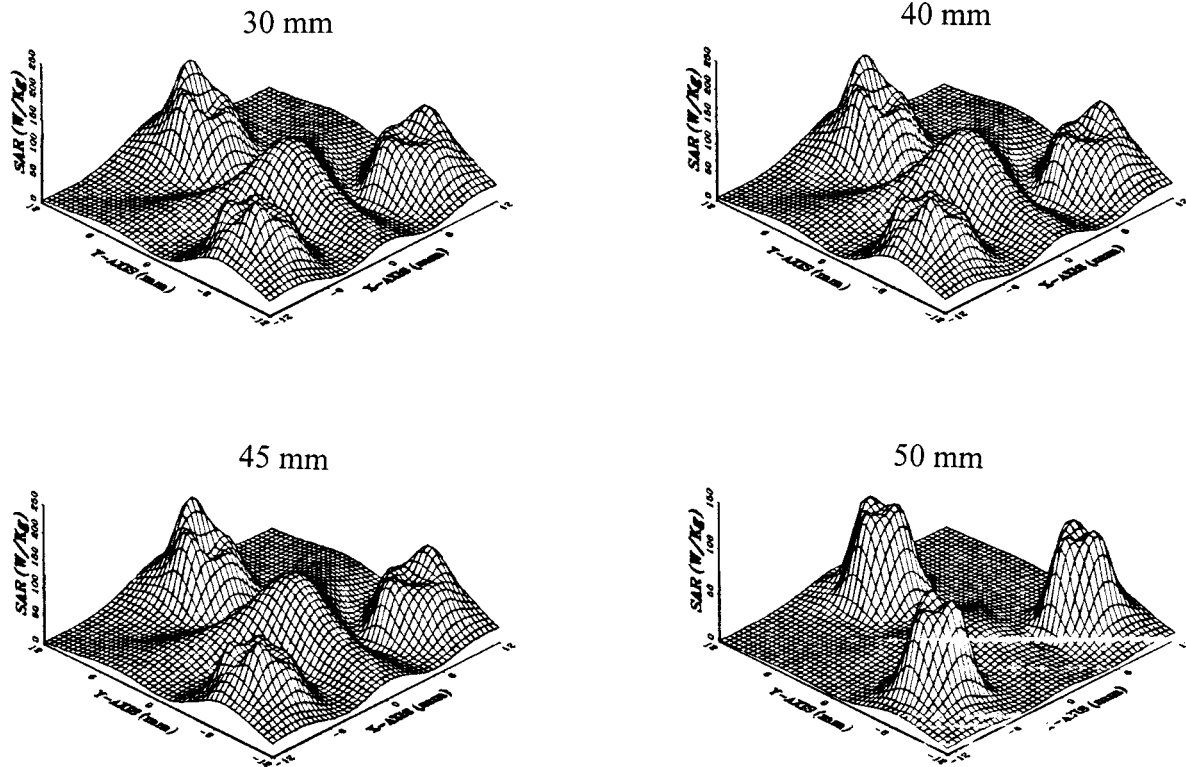
Fig. 5. SAR distributions computed over the transvere plane at 30, 40, 45, and 50 mm of a 15-mm equilateral triangle array.

A representative set of computed SAR distributions over the transverse plane at 30, 40, 45, or 50 mm for 15-mm spacing of a triangular array is shown in Fig. 5. Note that SARs peak at the array centers. These results show relatively low SARs at the 50-mm plane, which is beyond the tip of the antennas at 45 mm. The measured SAR distributions for equilateral triangular arrays of three sleeved-slot antennas spaced at 15 mm apart in phantom, likewise showed peak SARs at the array center Fig. 6.

Measured longitudinal SAR distributions inside the 15-mm array at a point (2.5 mm) close to the antennas and at the array center are given in Figs. 7 and 8, respectively. Note from Fig. 7, the enhanced SARs over the active region of antenna. A peak appeared near the tip with a plateau region of high SAR along the active length of the antennas and then tapering rapidly to a low SAR along the transmission-line feed. As can be seen from Fig. 8, SARs remain elevated over an extended length (about 35 mm from 10 to 45 mm at the 50% SAR point) along the central axis of the triangular array.

B. Hexagonal Arrays

SAR distributions in homogeneous brain tissue models have been computed for six- and seven-antenna hexagonal arrays formed by 15-mm equilateral triangular arrays. In the case of a six-element array, the central antenna was left out of the catheter. The computed SAR patterns at transverse cross sections 30, 40, 45, and 50 mm (which encompass the active region) from the air–tissue interface are shown in Fig. 9 for a hexagonal array of six antennas. The antenna tips are located at a depth of 45 mm from the surface. It can be seen that elevated SARs occur near the center of the array. Also, even without the

central antenna, there are additional peaks near the centers of the six virtual equilateral triangles formed by the antennas.

A similar set of measured cross-sectional SAR distributions are given in Fig. 10 for a six-element hexagonal array.

The addition of a seventh antenna at the center gave rise to computed and measured SAR patterns for seven-element hexagonal arrays are similar to those shown in Figs. 9 and 10, except for a higher SAR surrounding the central antenna.

A comparison of computed SAR distributions produced by six- and seven-element configurations is given in Table II. For both hexagonal array configurations, SAR variations are normalized to that at the center of the seven-element array. Note that in the center of a six-antenna array, SAR at 35 mm is higher than at the other two depths shown. However, for a seven-antenna array, the tip plane at 45 mm exhibits a higher value. The average SAR at the array center and range of variation produced by the six-element array is slightly lower than that by the seven-element array.

IV. DISCUSSION

The computer simulated and experimentally measured results are in general agreement, although their numerical values were not always the same. In particular, SAR distributions at all cross sections for the 15-mm array showed comparable trends for SARs at the array center and near the antennas. This suggests that a triangular array spacing of 15 mm has the least SAR variations for the miniature sleeved-slot microwave antennas operating at 2450 MHz. Moreover, Figs. 6 and 7 show the SAR near the air–tissue interface (0 mm) is about 25% of the maximum
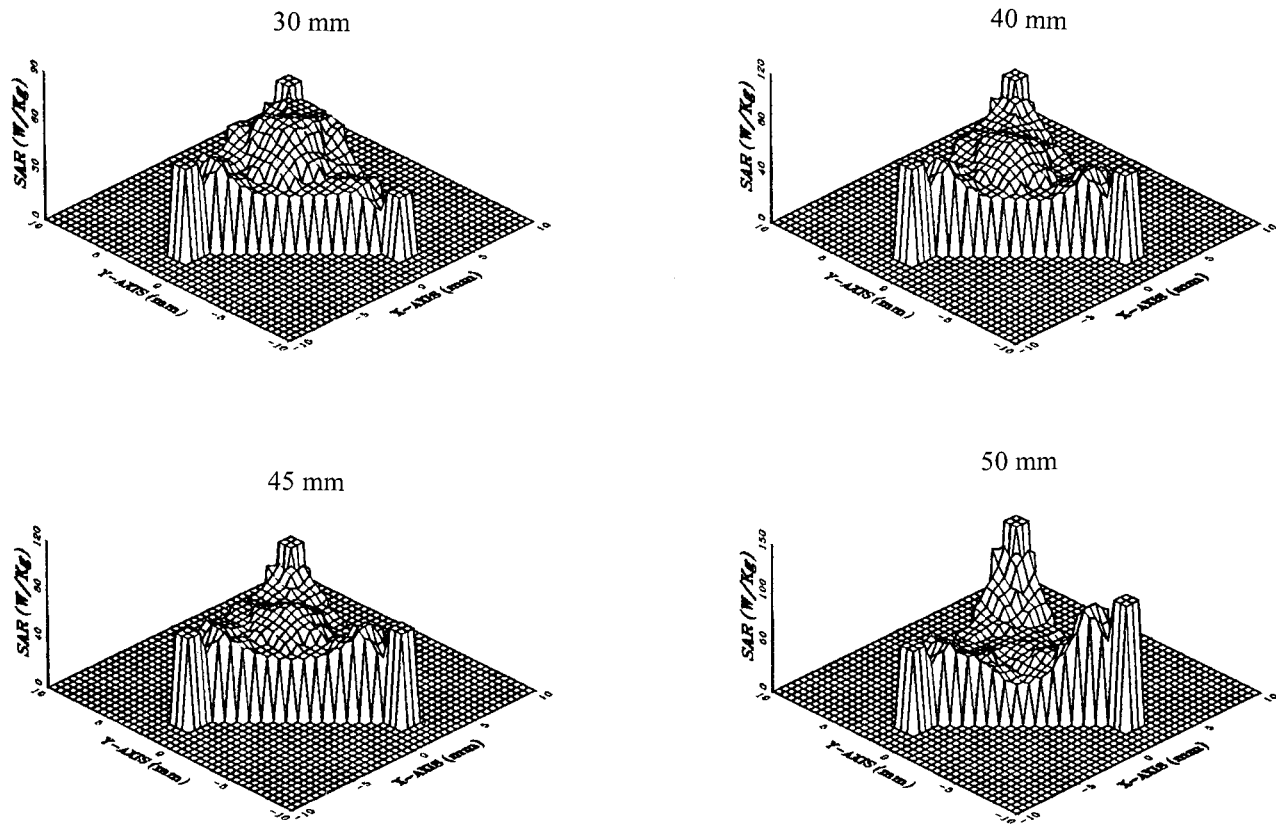
Fig. 6.   Measured SAR distributions in the transverse planes at 30, 40, 45, and 50 mm of a 15-mm equilateral triangle array of sleeved-slot antennas operating at 2450 MHz. The tips of the antennas are located at 45 mm.
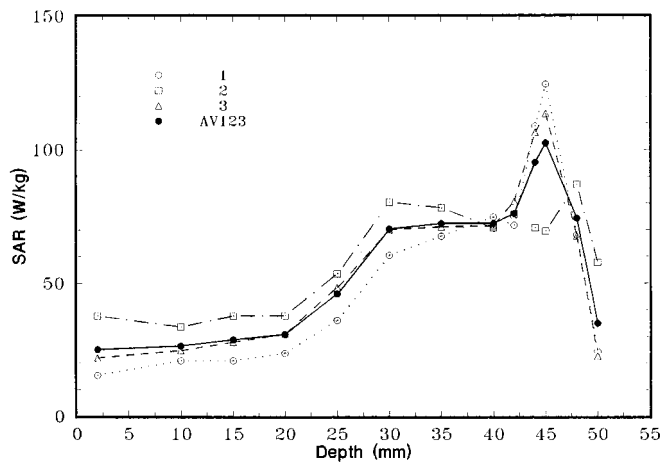

Fig. 7.   Measured longitudinal SAR distributions in a 15-mm equilateral triangle array of sleeved-slot antennas. The tips of the antennas are located at 45 mm. Values are for points at 2.5 mm from each antenna (an intermediate point inside the array). There appeared to be a slight misalignment of the fiber-optic sensors during the collection of data set #2.

Fig. 8.   Measured longitudinal SAR distributions at the array center inside the 15-mm triangular array.

value in phantom tissue. It is significant to note that while the SAR drops rapidly toward the surface of the tissue phantom, its distribution extends further (about 35 mm at 50% SAR) along the array center. Thus, the use of sleeved-slot antennas for the triangular array would produce a more uniform SAR distribution in a volume that includes the tip of the antennas.
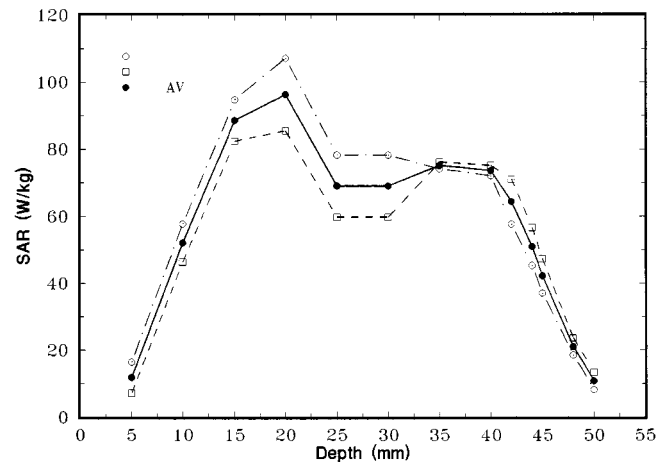
Accordingly, a 15-mm array spacing is selected for studying SAR distributions produced by six- and seven-element array configurations.

In principle, the three-element array configuration may be advantageous for irregular tumor geometries. The triangular configuration is more easily adaptable to conform to such geometries. For example, a hexagon is formed by a combination of equilateral triangles. Thus, the 15-mm triangular array could
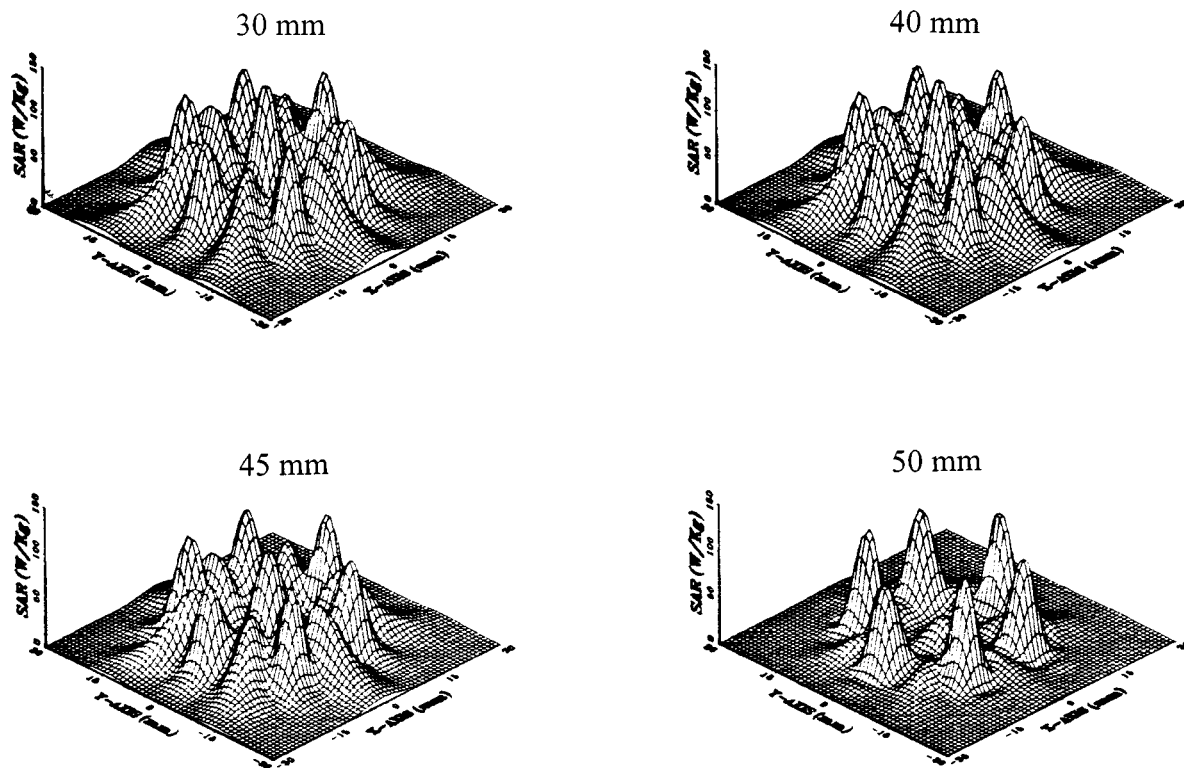
Fig. 9.   Computed SAR patterns for a hexagonal array of six antennas at transverse cross sections 30, 35, 45, and 50 mm from the air–tissue interface.
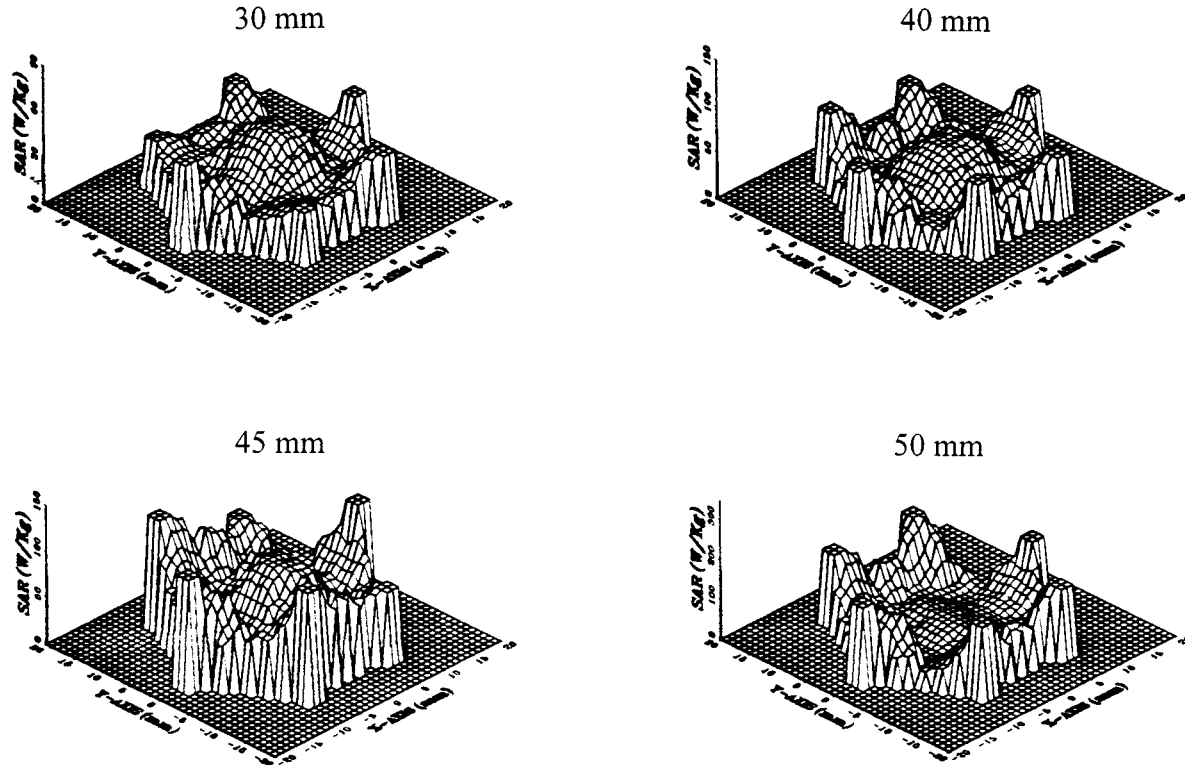

Fig. 10.   Measured cross-sectional SAR distributions for the six-element hexagonal array.

serve as an efficient building block to form hexagonal or other arrays of interstitial antennas for hyperthermia treatment of larger tumors.

As shown in Figs. 9 and 10, there is a general agreement between computer simulation and experimental measurement both for six- and seven-element hexagonal arrays. The average SAR

TABLE II
COMPARISON OF SAR VARIATION (PERCENTAGE) PRODUCED BY SIX- AND
SEVEN-ELEMENT HEXAGONAL ARRAYS INTERSTITIAL SLEEVED-SLOT
MICROWAVE ANTENNAS IMPLANTED TO A TIP DEPTH OF 45 mm

Depth (mm)	6-element array		7-element array	
	Range of Variation	Center	Range of Variation	Center
25	0.00 - 23.6	22.2	0.02 - 38.9	16.7
35	0.02 - 63.8	60.3	0.05 - 92.2	43.9
45	0.00 - 112	29.9	0.03 - 116	100
Average	0.01 - 66.5	37.5	0.03 - 82.4	53.5

Normalized to SAR in the center at 45 mm of a 7-element array.

at the array center and range of variation produced by the six-element array is slightly lower than the seven-element array (see Table II). Since the six-element array can provide SARs nearly as high as the seven-element array, but with lower SAR variation, suggests that it could provide more uniform SAR distribution using 2450-MHz sleeved-slot microwave antennas.

Although not part of this investigation, it is conceivable that incorporation of amplitude and phase variations into the feeding network for the antennas could further improve the uniformity. However, the most important use of phased arrays would be to steer the SAR distribution inside the tissue, which is beyond the cope of this paper.

It is noted that, in clinical practice, information on temperature distribution is also of interest. In order to conduct a full investigation of the dynamic temperature change, one needs to take into account tissue composition, blood perfusion, heat conduction effects of various tissues, and heat generation due to metabolic processes. Although several vascular models have been proposed to predict precise temperature distributions [16], [17], a clinical usefulness model is still under development. It is anticipated that continued development could provide the detailed information required of an anatomically based hyperthermia treatment planning system. Indeed, a project is underway in our laboratory to assess the temperature distribution produced by interstitial sleeved-slot antenna arrays using the finite-difference formulation of the bioheat transfer equation. It is our hope that the computer simulations of induced temperature distribution together with animal experimentation will help us to arrive at an optimal set of conditions for a sufficiently uniform temperature distribution in the near future. Nevertheless, it should be mentioned that SAR distribution is the instantaneous microwave power deposition that causes tissue temperature to rise and, under normal circumstances, SAR is not impacted by the list of factors that influence the dynamics of temperature distribution.

V. CONCLUSION

Through computer simulation and experimental measurement, we have investigated equilateral triangular and hexagonal arrays of sleeved-slot interstitial microwave antennas to produce SAR distributions. For 2450-MHz operation of three sleeved-slot antennas with equal amplitude and phase, an array spacing of 15 mm would provide a more uniform SAR distribution when compared to both smaller or larger array spacings. Moreover, the region of elevated SAR is inscribed by the width of the antenna arrays and extends 35 mm in length to include the distal antenna-tip region. In addition, results indicate that a hexagonal array configuration of either six or seven sleeved-slot interstitial antennas could provide elevated SARs in brain tissues. Since the six-element configuration uses one less interstitial antenna with comparable SARs, it offers a better scheme for hyperthermia treatment of brain tumors.

REFERENCES

[1] M. H. Seegenschmiedt, P. Fessenden, and C. C. Vernon, Eds., *Thermoradiotherapy and Thermochemotherapy, Vol. 1, Biology, Physiology and Physics.* Berlin, Germany: Springer-Verlag, 1995.

[2] ——, *Thermoradiotherapy and Thermochemotherapy, Vol. 2, Clinical Applications.* Berlin, Germany: Springer-Verlag, 1996.

[3] J. H. Suh and G. H. Barnett, "Brachytherapy for brain tumor," *Hematol. Oncol. Clin. North Amer.*, vol. 13, pp. 635–650, 1999.

[4] J. Overgaard, D. G. Gonzalez, M. C. C. M. Hulshof, G. Arcangeli, O. Dahl, O. Mella, and S. M. Bentzen, "Randomised trial of hyperthermia as adjuvant to radiotherapy for recurrent or metastatic malignant melanoma," *Lancet*, vol. 345, pp. 540–543, 1995.

[5] ——, "Hyperthermia as an adjuvant to radiation therapy of recurrent or metastatic malignant melanoma—A multicentre randomized trial by the European Society for Hyperthermic Oncology," *Int. J. Hyperthermia*, vol. 12, pp. 3–20, 1996.

[6] H. Kuwano, K. Sumiyoshi, M. Watanabe, N. Sadanaga, T. Nozoe, M. Yasuda, and K. Sugimachi, "Preoperative hyperthermia combined with chemotherapy and irradiation for the treatment of patients with esophageal carcinoma," *Tumori.*, vol. 81, pp. 18–22, 1995.

[7] B. Stea, J. Kittleson, and J. R. Cassady, "Treatment of malignant glioma with interstitial irradiation and hyperthermia," *Int. J. Radiat. Oncol. Biol. Phys.*, vol. 24, pp. 657–667, 1992.

[8] T. Nakajima, D. W. Roberts, T. P. Ryan, P. J. Hoopes, C. T. Coughlin, B. S. Trembly, and J. W. Strohbehn, "Pattern of response to interstitial hyperthermia and brachytherapy for malignant intracranial tumour: A CT analysis," *Int. J. Hyperthermia*, vol. 9, pp. 491–502, 1993.

[9] B. Emami, C. Scott, C. A. Perez, S. Asbell, P. Swift, P. Grigsby, A. Montesano, P. Rubin, W. Curran, J. Delrowe, H. Arastu, K. Fu, and E. Moros, "Phase III study of interstitial thermoradiotherapy compared with interstitial radiotherapy alone in the treatment of recurrent or persistent human tumors—A prospectively controlled randomized study by the Radiation Therapy Oncology Group," *Int. J. Radiat. Oncol. Biol. Phys.*, vol. 34, pp. 1097–1104, 1996.

[10] P. K. Sneed, P. R. Stauffer, M. W. McDermott, C. J. Diederich, K. R. Lamborn, M. D. Prados, S. Chang, K. A. Weaver, L. Spry, M. K. Malec, S. A. Lamb, B. Voss, R. L. Davis, W. M. Wara, D. A. Larson, T. L. Phillips, and P. H. Gutin, "Survival benefit of hyperthermia in a prospective randomized trial of brachytherapy boost +/− hyperthermia for glioblastoma multiforme," *Int. J. Radiat. Oncol. Biol. Phys.*, vol. 40, pp. 287–295, 1998.

[11] J. C. Lin and Y. J. Wang, "Interstitial microwave antennas for thermal therapy," *Int. J. Hyperthermia*, vol. 3, pp. 37–47, 1987.

[12] W. L. Stutzman and G. A. Thiele, *Antenna Theory and Design.* New York: Wiley, 1981, ch. 1.

[13] M. F. Iskander and A. M. Tumeh, "Design optimization of interstitial antennas," *IEEE Trans. Biomed. Eng.*, vol. 36, pp. 238–246, Feb. 1989.

[14] J. C. Lin, "Engineering and biophysical aspects of microwave and radiofrequency radiation," in *Hyperthermia*, D. J. Watmough and W. M. Ross, Eds. Glasgow, Scotland: Blackie, 1986, pp. 42–75.

[15] A. W. Guy, "Analysis of electromagnetic fields induced in biological tissues by thermographic studies on equivalent phantom models," *IEEE Trans. Microwave Theory Tech.*, vol. MTT-19, pp. 205–214, Feb. 1971.

[16] J. W. Baish, P. S. Ayyaswamy, and K. R. Foster, "Heat transport mechanisms in vascular tissues: A model comparison," *J. Biomech. Eng.*, vol. 108, pp. 324–331, 1986.

[17] J. Crezee and J. J. W. Lagendijk, "Temperature uniformity during hyperthermia: The impact of large vessels," *Phys. Med. Biol.*, vol. 37, pp. 1331–1337, 1992.

James C. Lin (S'65–M'67–SM'77–F'86), photograph and biography not available at time of publication.

Shinji Hirai, photograph and biography not available at time of publication.

Chin-Lin Chiang, photograph and biography not available at time of publication.

Wen-Lin Hsu, photograph and biography not available at time of publication.

Jenn-Lung Su (S'84–M'84), photograph and biography not available at time of publication.

Yu-Jin Wang, photograph and biography not available at time of publication.